Microporous and Mesoporous Materials 153 (2012) 247–253

Contents lists available at SciVerse ScienceDirect

Microporous and Mesoporous Materials

journal homepage: www.elsevier.com/locate/micromeso

Mesoporous manganese dioxide prepared under acidic conditions as high performance electrode material for hybrid supercapacitors

Yu-Ting Wang, An-Hui Lu, Wen-Cui Li *

State Key Laboratory of Fine Chemicals, School of Chemical Engineering, Dalian University of Technology, Dalian 116024, PR China

ARTICLE INFO

Article history:
Received 4 July 2011
Received in revised form 13 December 2011
Accepted 2 January 2012
Available online 8 January 2012

Keywords:
Mesoporous materials
Hybrid supercapacitor
Manganese dioxide
Birnessite
Acid treatment

ABSTRACT

High surface area mesoporous manganese dioxide (MnO_2) with α-phase crystalline structure has been synthesized by the reduction of potassium permanganate with ethylene glycol under acidic conditions. Nitrogen sorption analyses show that MnO_2 synthesized under acidic conditions exhibits a type IV isotherm, indicating a mesoporous character. Electrochemical performances of MnO_2 samples as supercapacitor electrode materials have been studied in a three-electrode system. A hybrid supercapacitor based on using a composite material (MnO_2&Activated Carbon) as the positive electrode and activated carbon as the negative electrode has been fabricated. The hybrid supercapacitor fabricated using MnO_2 synthesized under acidic conditions has excellent large current charge–discharge performance, and shows a practical cell voltage of 1.8 V and a capacitance of 22.1 F g^{-1} after 1500 cycles even in the presence of the dissolved oxygen. MnO_2 synthesized in the absence of acid shows poor cycle performance and a low capacitance.

1. Introduction

Supercapacitors with a high power density and long-cycle life have been commercially used as power sources of various devices. Recently, much attention is aimed at increasing the energy density and reducing the fabrication costs of the supercapacitors due to the rapid development of electric cars. The use of organic electrolytes in supercapacitors can provide a wider and stable electrochemical operation window and thus contribute a relatively high energy density. However, they suffer from the use of highly toxic and/or flammable solvents which can cause severe safety hazards. Fortunately, in aqueous-based systems, the relatively small voltage range can be partially compensated by the use of a hybrid system which relies on the positive and negative electrodes consisting of different materials that have a different potential range of electroactivity [1,2].

Generally, in hybrid supercapacitors, the negative electrodes consist of porous carbon. Various metal oxides with pseudocapacitive properties instead of materials with only capacitive properties can be used as positive electrodes that give an increase in the energy density of the hybrid supercapacitor, thus enlarging the working potential window [3–5]. Among them, hydrated ruthenium dioxide ($RuO_2{\cdot}xH_2O$) shows the highest specific capacitance (>720 F g^{-1}) [6]. The main disadvantage of $RuO_2{\cdot}nH_2O$ is its high cost and toxicity. Therefore, currently considerable effort has been devoted to identify alternative and inexpensive electrode materials with acceptable electrochemical performance.

Manganese dioxide (MnO_2) is a good candidate due to its low cost and the fact that manganese can be considered more environmentally friendly than other transition metals [7,8]. Furthermore a variety of synthetic methods such as hydrothermal reaction [9], thermal decomposition [10], electro-deposition [11], template method [12], micro-emulsion method [13], etc. can be utilized to tailor the crystalline phases and morphologies of MnO_2 electrode materials. Therefore, much attention has been paid to develop MnO_2-based hybrid supercapacitors. Hong et al. [14–16] investigated a hybrid system with a positive MnO_2-based electrode and a carbon negative electrode. An operating voltage of 2 V was demonstrated for this hybrid capacitor in a neutral KCl aqueous electrolyte. We recently also reported a hybrid supercapacitor using MnO_2 mixed with tiny amount of commercial activated carbon as positive electrode and this activated carbon as negative electrode. An improved capacitance can be achieved due to the use of activated carbon in MnO_2 positive electrode [17]. It is known that, for an electrode to perform effectively in a supercapacitor cell, access of the electrolyte to as much of the internal and external electrode surface as possible is desirable. Thus attempts are often made to synthesize MnO_2 with the highest possible surface area and suitable pore size [7,18]. High surface area is beneficial for a high capacitance, while a suitable pore size facilitates ion transport through the electrolyte. This enhances the electrochemical performance.

* Corresponding author. Tel./fax: +86 411 84986140.
E-mail address: wencuili@dlut.edu.cn (W.-C. Li).

1387-1811/$ - see front matter © 2012 Elsevier Inc. All rights reserved.
doi:10.1016/j.micromeso.2012.01.004

In this paper we report a simple and fast synthesis of mesoporous MnO_2 via the reaction of potassium permanganate with ethylene glycol under acidic conditions. The highlight of the current work is that when a certain amount of acid is added in the reaction system, the resultant MnO_2 in a hybrid supercapacitor shows high electrochemical performance even after 1500 cycles and in the presence of the dissolved oxygen, while MnO_2 synthesized without acid addition showed poor cycle performance and low capacitance.

2. Experimental

2.1. Sample preparation

All chemicals used in this study were of analytical grade, and used without further purification. In a typical experiment, 5.5 mmol (0.865 g) of $KMnO_4$ was dissolved in 50 ml of deionized water and stirred with a magnetic stirrer for 30 min to form a homogeneous solution at room temperature, and then mixed with 22.5 mmol (1.25 ml) of ethylene glycol. The mixture was aged for 20 min on stirring at ambient conditions. The deposits were collected by centrifugation, washed several times with deionized water and absolute ethanol until the pH of the wash was neutral, and then dried at 60 °C for overnight under air atmosphere. This sample was denoted as MnO_2-0 for the following tests. While in the remaining three experiments, 1, 3 and 5 ml concentrated sulfuric acid were added in the ethylene glycol solution, respectively, and aged for 20 min on stirring at ambient conditions. The collected samples were correspondingly denoted as MnO_2-1, MnO_2-3 and MnO_2-5 for the following tests. To see the stability of the sample, MnO_2-1 was heated at an interval of 100 °C for 2 h starting from 200 up to 400 °C, and the collected samples were denoted as MnO_2-200, MnO_2-300 and MnO_2-400, respectively.

The working electrodes of electrochemical capacitors were fabricated by mixing MnO_2 powder with 20 wt.% acetylene black conductor and 10 wt.% poly(tetrafluoroethylene) (PTFE) binder. A small amount of ethanol was then added to this mixture followed by an ultrasonication treatment for 1 h. The homogenized mixture was pressed onto a stainless steel current collector ($1.0 \times 1.0\ cm^2$) to fabricate an electrode.

2.2. Characterization

Power X-ray diffraction (XRD) measurements were taken on a Rigaku D/Max 2400 diffractometer using CuK_α radiation (40 kV, 100 mA, $\lambda = 0.15406$ nm). Scanning electron microscopy (SEM) images were obtained from a Hitachi S-4800 instrument. Surface area and porosity was determined by nitrogen adsorption at 77 K using a Micromeritics ASAP 2020 Analyzer. Prior to analysis, all samples were degassed under vacuum at 80 °C for at least 4 h. The specific surface area was calculated using the BET method, while the pore size distribution (PSD) curves were calculated from the desorption branches based on the Barrett–Joyner–Halenda (BJH) equation. Thermogravimetric analysis (TGA) was carried out in the temperature range from room temperature to 600 °C in air with a heating rate of 10 °C min^{-1} using a STA 449 F3 Jupiter thermogravimetric analyzer (NETZSCH).

The electrochemical performances of MnO_2-based electrodes were tested using a cyclic voltammetry (CV) method and a constant current charge/discharge test. All electrochemical measurements were carried out in 0.5 M Na_2SO_4 aqueous electrolyte solution at room temperature with a conventional three-electrode electrochemical setup in which the MnO_2 electrode was served as working electrode, a slice of platinum sheet was used as auxiliary electrode and a saturated calomel electrode (SCE) as reference electrode. All electrochemical experiments were carried out at room temperature.

Besides evaluation in the three-electrode system, the electrochemical performance of MnO_2 in the two-electrode system have also been conducted by using commercial activated carbon (AC) as negative electrode and MnO_2 mixed with tiny amount of AC composite (MnO_2&AC) as positive electrode in 0.5 M Na_2SO_4 electrolyte. The negative electrode was prepared using AC (YP/47, specific surface area of ca. 1870 $m^2\ g^{-1}$, Japan) mixed with poly(tetrafluoroethylene) (PTFE) in a weight ratio of 90:10 pressed onto a stainless steel grid. The positive electrode was prepared by pressing a powdered mixture of MnO_2, AC, acetylene black and PTFE in a weight ratio of 70:10:10:10 onto a stainless steel grid. A two-electrode cell was tested on Arbin SCTS-5V5A 8CH.

3. Results and discussion

As potassium permanganate and ethylene glycol (EG) are strong oxidizing agent and reducing agent, respectively, the exothermic redox reaction leads to the formation of MnO_2 and other oxidized products, such as aldehydes or a mixture of aldehydes, carboxylic acids and even CO_2 is produced. The formation process may be explained as follows: Once ethylene glycol was added into $KMnO_4$ acid solution, MnO_2 nuclei was formed immediately, which acted as the precursor. The chemical reaction can be formulated as:

$$\begin{aligned} &OH{-}H_2C{-}CH_2{-}OH + MnO_4^- + H^+ \rightarrow MnO_2 + X + H_2O \\ &X = \text{glyoxal, oxalic acid, } CO_2 \text{ or a mixture of them} \end{aligned} \quad (1)$$

When no sulfuric acid was added in the solution, the pH was ca. 6. If 1 ml sulfuric acid was added, the pH dropped to 0.5–1, and when 3 ml, 5 ml sulfuric acid were added, the pH kept at 0.1–0.5. Concentrated sulfuric acid added in the solution increased the oxidizability of potassium permanganate, so that the reaction rate was further increased. On the other hand, acid can also "etch" the originally produced manganese dioxide [19], thereby increasing the specific surface area (this is evidenced from the nitrogen sorption data).

3.1. Effect of the amount of acid on the structure of MnO_2

The samples MnO_2-1, MnO_2-3 and MnO_2-5 were prepared by adding 1, 3 and 5 ml, respectively of concentrated sulfuric acid in the reaction conditions. As a comparison, MnO_2-0 was prepared without sulfuric acid. Structural analysis was carried out using powder XRD. Fig. 1 shows the powder XRD pattern of the as-prepared

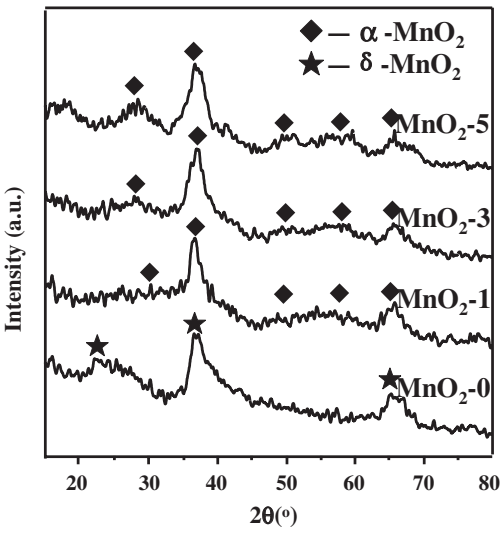

Fig. 1. Powder XRD patterns of MnO_2-0, MnO_2-1, MnO_2-3 and MnO_2-5.

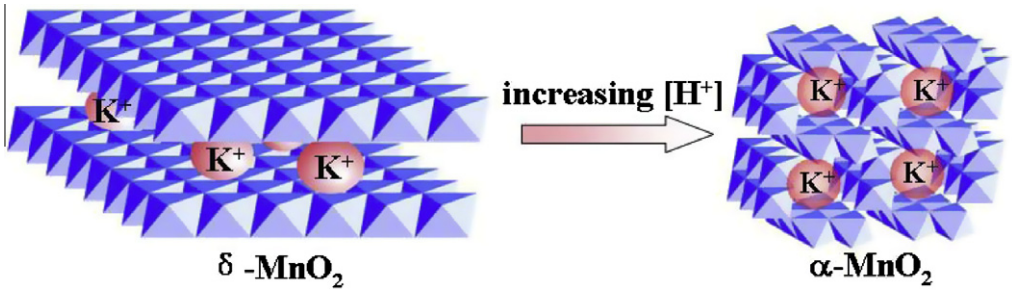

Fig. 2. Schematic diagram of manganese dioxide structural transitions induced during synthesis.

MnO_2. The broad reflections indicate that the particle sizes of the samples are small. In Fig. 1 broad peaks at $2\theta = 24.8°$, 37.0°, and 65.4° in the MnO_2-0 pattern correspond to δ-MnO_2, while in the other three patterns significant XRD peaks at $2\theta = 28.5°$, 36.8°, 50.1°, 60.2° and 65.7° are assigned to α-MnO_2. That is to say, as acid was added in the reaction system, the crystalline phase of MnO_2 was gradually transferred from a 2D layered δ-phase crystalline structure to a 1D tunnel α-phase crystalline structure.

We speculate that the cation concentration in solution might affect the phase transition of MnO_2. The amount of $KMnO_4$ was superfluous in the reaction process, and the presence of excess K^+ ions can stabilize the 2D layered δ-structure of MnO_2. This is to say, birnessite derives its structural stability from the presence of foreign metal ions (e.g., K^+, Na^+, in the present case) between the layers of MnO_6 octahedra, since without these species the structure collapses to a tunnel structure [20]. After adding the sulfuric acid, there is a competition between the foreign metal ions and protons for the same sites in the newly formed manganese dioxide structure. When suitable foreign metal ions are in excess, a templating effect predominates to form birnessite. When protons are in excess, however, the structure collapses to form tunnels (Fig. 2).

The effect of acid on the morphologies of the products was investigated using SEM. As shown in Fig. 3a and b, MnO_2-0 is composed of spherical aggregates of nanoparticles without clear interparticle boundaries. A mass of particles agglomerates together to form large conglomerates on the MnO_2-0 surface. SEM picture for the material synthesized in acidic conditions are shown in Fig. 3c–f. MnO_2-1 (Fig. 3c and d) is composed of agglomerated nanorods with an average length of ca. 25 nm. The morphology of the particles is shown as a mixture of a few of nanorods and nanostructured surface with a distinct plate-like morphology. The well defined regions of the nanoplate exhibit definite pores which will play an important role in the redox process when used as an electrode material in a supercapacitor.

As shown in Fig. 4a, the nitrogen sorption isotherm of the resultant MnO_2-0 exhibits a hysteresis loop in the relative pressure range above 0.90, and no plateau appears in the adsorption branch, indicating the existence of macropores. The nitrogen sorption isotherms of MnO_2-1, MnO_2-3 and MnO_2-5 are of type IV, displaying hysteresis loops in the relative pressure range of 0.7–0.9 and plateaus appeared in the adsorption branches, indicating the mesoporous nature. With an increasing amount of acid, the hysteresis loops move to a lower relative pressure range, reflecting a decrease in pore size. The corresponding pore size distribution curves (Fig. 4b) indicate that MnO_2-0 sample has no centralized pore size distribution while MnO_2-1, MnO_2-3 and MnO_2-5 have narrow pore size distributions with mesopore sizes concentrated at ca. 10 nm.

The calculated texture parameters of these MnO_2 nanoparticles are compiled in Table 1. It can be seen that the BET surface area of sample MnO_2-0 is 150 $m^2\ g^{-1}$ and pore volume 0.42 $cm^3\ g^{-1}$, while the surface area and pore volume of the MnO_2 synthesized under acidic conditions significantly increased. It should be noted that, the stronger the acidity of potassium permanganate, the stronger its oxidizability, and the faster reaction rate. Besides acid can dissolve MnO_2 nanoparticles, so the product yield became more and more lower. As shown in Table 1 the product yields of MnO_2-3 and MnO_2-5 are so low that their thermal stability and electrochemical properties cannot be investigated any more.

3.2. Thermal stability of the prepared MnO_2

It is known that thermal treatment for manganese oxide can cause a loss of surface area and phase change. Therefore, it is necessary to find an optimal thermal treatment condition in order to maintain the MnO_2 phase with acceptable surface area. The thermal decomposition behavior of MnO_2 was analyzed and the TG/DSC curves of the as-prepared MnO_2-1 are shown in Fig. 5. The sample shows a distinct weight loss (~10 wt.%) upon heating from room temperature to 200 °C, which is accompanied by a sharp exothermic peak at approximately 200 °C, indicating the loss of water molecules which exist both on the surface and in the lattice of the nanostructure. Subsequently, a slight weight loss less than 3% occurs in the temperature range of 200–520 °C. Finally, a weight loss of 4% appeared at a temperature of 520 °C, and a broad exothermic peak was found at approximately 550 °C.

Following the TG/DSC analysis, sample MnO_2-1 was calcined at temperatures of 200, 300 and 400 °C, for 2 h to investigate its phase transition. Fig. 6 shows the XRD patterns of the calcined samples. According to the XRD patterns, the structure remained unchanged after heating at 200 °C for 2 h, indicating that the dehydration of the crystal water did not cause damage to the structure. The increase in intensity of the peaks with temperature shows a gradual evolution to a crystalline phase. A highly crystalline sample was obtained at 300 °C and 400 °C, and all the diffraction peaks correspond to Mn_3O_4.

The nitrogen sorption isotherms and the pore size distributions of the calcined samples are shown in Fig. 7. As seen in Fig. 7a the isotherm of sample MnO_2-200 with a hysteresis loop at the relative pressure (P/P_0) range of 0.7–0.95 is similar to that of MnO_2-1, indicating the porous structure of MnO_2 is essentially unchanged. With increasing calcination temperature, the isotherms of MnO_2-300 and MnO_2-400 remain type IV. However, the hysteresis loops progressively decrease in size and move to higher relative pressures, reflecting the formation of large mesopores or macropores. The adsorbed volume also gradually decreases, corresponding to a lower surface area and pore volume (see Table 1). Pore size distributions of MnO_2 (Fig. 7b) show that the calcined MnO_2 samples have wide pore size distributions.

3.3. Electrochemical performance of MnO_2 in three-electrode system

Electrochemical performance of the prepared MnO_2 material was firstly studied by cyclic voltammetry (CV) which is considered

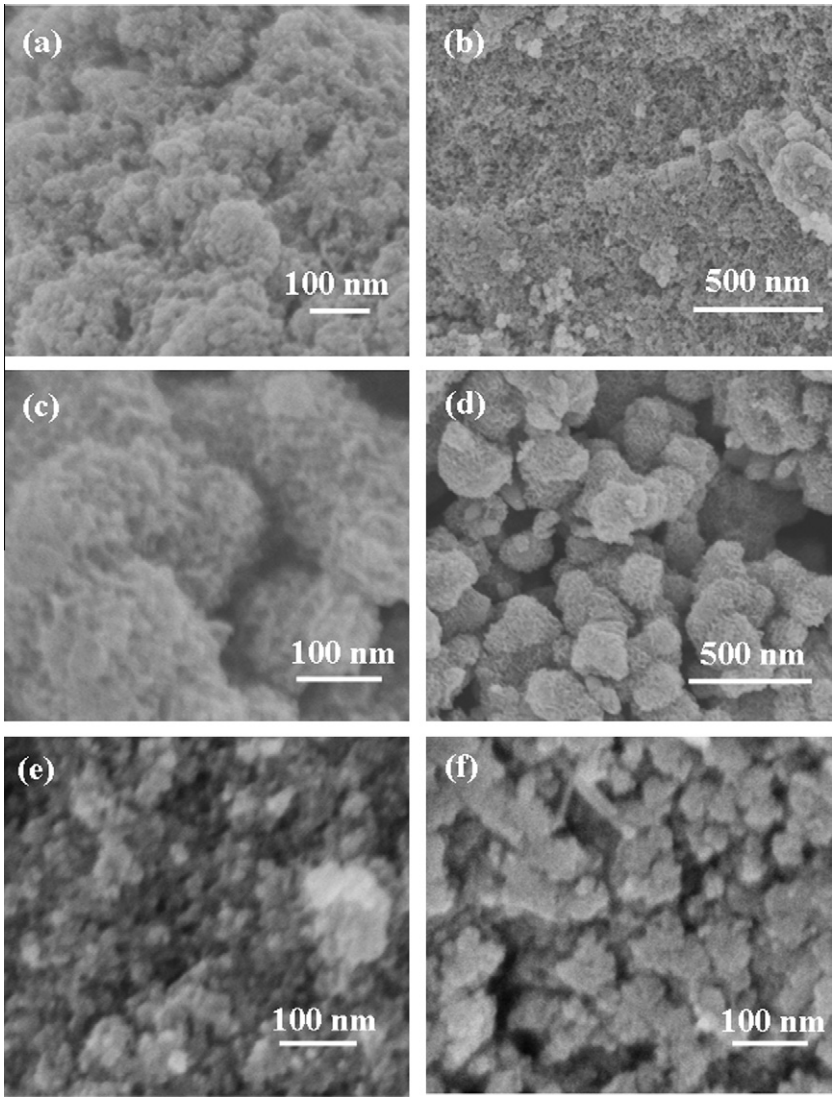

Fig. 3. SEM images of as-prepared MnO_2-0 (a, b), MnO_2-1 (c, d), MnO_2-3 (e) and MnO_2-5 (f).

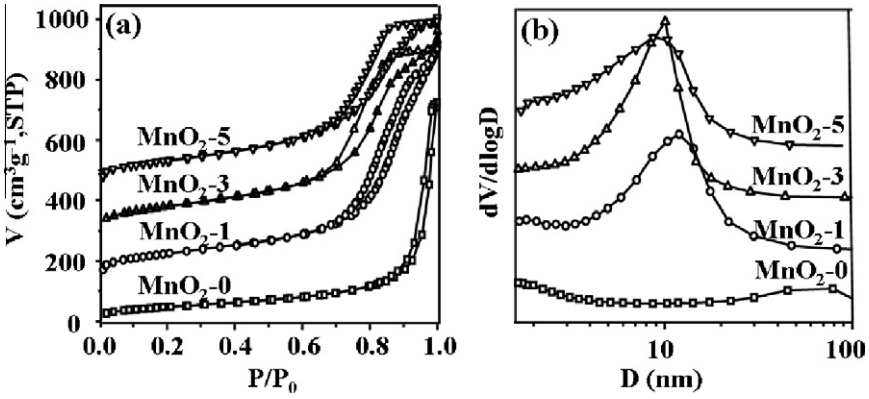

Fig. 4. Nitrogen sorption isotherms (a) and pore size distributions (b) of MnO_2 nanoparticles prepared with different amounts of acid. The isotherms of MnO_2-1 and MnO_2-3, MnO_2-5 were offset vertically by 150, 300 and 450 $cm^3\ g^{-1}$ STP, respectively.

to be an ideal experimental technique to study the capacitive behavior of any material. Fig. 8a shows CV plots of MnO_2-0, MnO_2-1 and the calcined samples in 0.5 M Na_2SO_4 electrolyte at a scan rate of 5 mV s^{-1} in a potential range of 0–1.0 V. It can be seen that there are no sharp redox peaks over the potential range investigated. The rectangular voltammograms suggest an ideal capacitive behavior of the as-prepared MnO_2. It can be seen that MnO_2-0 sample shows similar or even higher charging current

Table 1
Texture parameters and electrochemical properties of MnO_2 prepared under different experimental conditions.

Sample	Yield (%)	Crystal phase	S_{BET}[a] ($m^2\ g^{-1}$)	V_{total}[b] ($cm^3\ g^{-1}$)	D_{peak}[c] (nm)	C[d] ($F\ g^{-1}$)	CE[e] (%)
MnO_2-0	~100	δ-MnO_2	150	0.42	–	185	96
MnO_2-1	60	α-MnO_2	270	1.03	12.3	170	96
MnO_2-3	19	α-MnO_2	289	1.01	9.5	–	–
MnO_2-5	10	α-MnO_2	293	0.82	8.4	–	–
MnO_2-200	–	α-MnO_2	197	1.03	16.5	145	98
MnO_2-300	–	Mn_3O_4	159	0.66	15.5	115	99
MnO_2-400	–	Mn_3O_4	97	0.49	19.2	85	98
AC[f]	–	–	1869	0.93	1.0	160	99

[a] BET specific surface area calculated over P/P_0 range 0.03–0.25.
[b] Total pore volume at $P/P_0 \sim 0.995$.
[c] The maximum BJH pore size distribution peak.
[d] The specific gravimetric capacitance measured by the galvanostatic charge–discharge at current density of 6.0 mA cm^{-2}.
[e] Columbic efficiency.
[f] Commercial activated carbon (YP/47, Japan).

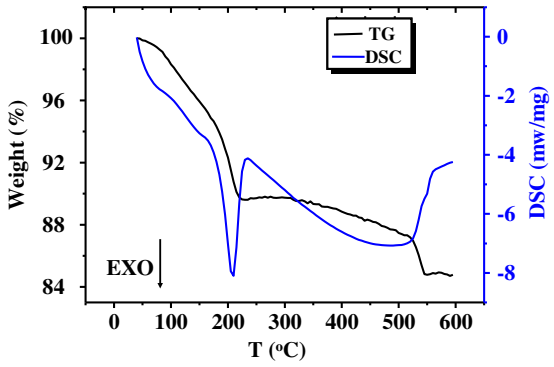

Fig. 5. TG and DSC curves of as-prepared MnO_2-1.

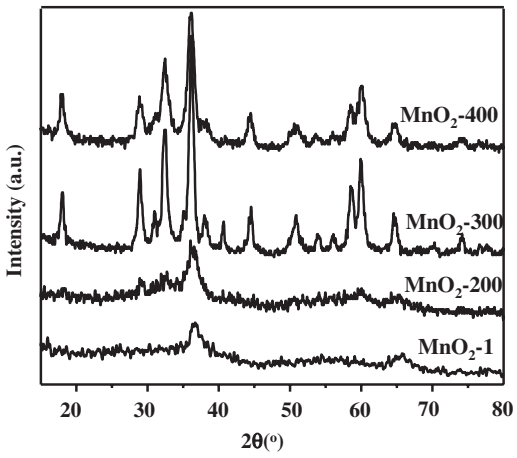

Fig. 6. Powder XRD patterns of as-prepared sample MnO_2-1 and its calcined samples (MnO_2-200, MnO_2-300 and MnO_2-400 were calcined at temperatures of 200, 300 and 400 °C respectively).

density compared with mesoporous MnO_2-1 sample, this is because, in lower current density, ion can easily reach the surface of the active material, so the superiority of MnO_2-1 over MnO_2-0 is unconspicuous. However, there is a slight decrease in specific capacitance for the samples heated at 200 °C compared to the original as-prepared MnO_2-1. For the samples heated at 400 °C, gradual decreases in specific capacitance are visible due to the decrease in specific surface area. A similar trend is found in the RuO_2 capacitor behavior [21]. When the samples are treated at lower temperature, the as-prepared MnO_2 with more adsorbed water and chemical hydration water has a hydrophilic surface structure, which can improve the protons/ions diffusion and adsorption/desorption during the redox transitions, so that more protons will immerse in electrode material surface or inside to participate in the redox reactions.

Typical charge–discharge curves in Fig. 8b reveal that the as-prepared MnO_2 exhibit stable electrochemical behavior as the capacitor voltage varies linearly with time during the charging and discharging process. This type of linear variation of potential is another important criterion for capacitance behavior of an electrode material. In Fig. 8b we can see, the performance of MnO_2-0 sample drops far behind MnO_2-1 sample, this is because the mass of the MnO_2-1 electrode slice is bigger than MnO_2-0, so it's discharge time is longer (it is consistent with Fig. 8a). In the high voltage range of the MnO_2-400 charge–discharge curves, the voltage drop is obvious and is a manifestation of a large internal resistance. Though a small amount of water is good for improving the electrode material activity, the inner resistance is another consideration for the comprehensive electrochemical properties. The calculated specific capacitance of MnO_2 is shown in Table 1.

3.4. Electrochemical performance of MnO_2 in hybrid supercapacitor

To study the electrochemical performance of MnO_2 in hybrid supercapacitors, we assembled a series of hybrid supercapacitors. Sample MnO_2-0, MnO_2-1, MnO_2-200 and MnO_2-300 were selected as the positive electrode materials to fabricate hybrid supercapacitors and the commercial activated carbon (AC) as negative electrode. In order to improve the electrical conductivity of the MnO_2 positive electrode material and achieve a high capacitance, we utilize a certain amount of activated carbon to mix with MnO_2, wherein the AC has the dual function of both a conductive agent and an active substance of a positive electrode. Thus, the fabricated hybrid supercapacitor is composed of MnO_2 and AC (MnO_2&AC) as the positive electrode and AC as the negative electrode, which integrates approximate symmetric and asymmetric behaviors in the distinct parts of 1.8 V operating windows [18,22]. That is, MnO_2&AC in the positive electrode and AC in the negative electrode together form an asymmetric structure, which extends the operating voltage to 1.8 V due to the compensatory effect of opposite over-potentials. In the range of −0.8 to 0 V, both AC in the positive and negative electrode assemble as a symmetric structure via a parallel connection which offers more capacitance and less internal resistance.

Fig. 9 shows the cyclic voltamogramms and potential *vs* time curves of the optimized hybrid AC–MnO_2&AC capacitors in 0.5 M Na_2SO_4 aqueous solution. It can be seen in Fig. 9a that the hybrid supercapacitors AC–MnO_2-1&AC, AC–MnO_2-200&AC and

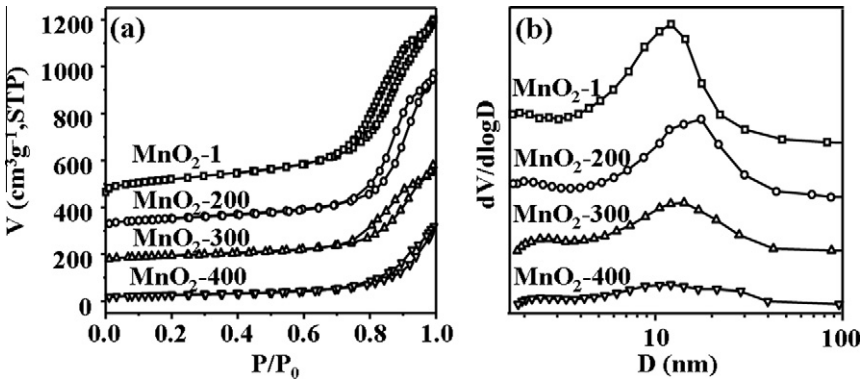

Fig. 7. Nitrogen sorption isotherms (a) and pore size distributions (b) of the as-prepared and calcined MnO_2 samples. The isotherms of MnO_2-300, MnO_2-200 and MnO_2-1 were offset vertically by 150, 300 and 450 $cm^3\ g^{-1}$ STP, respectively.

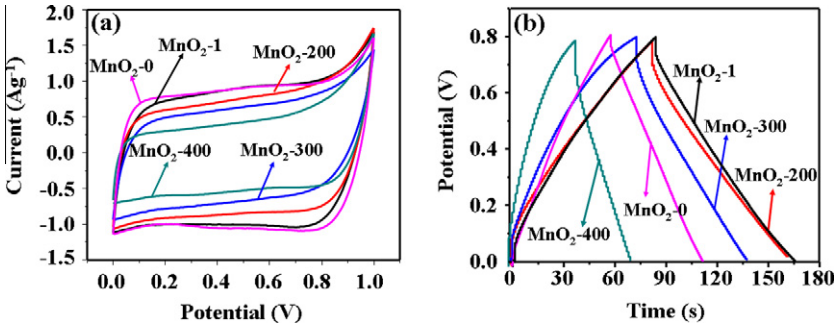

Fig. 8. Cyclic voltammograms in 0.5 M Na_2SO_4 at a scan rate of 5 mV s^{-1} (a), Charge–discharge curves of the first 10 cycles at a constant current density 6 mA cm^{-2} (b) of the as-prepared and calcined MnO_2 samples (MnO_2-0: magenta line; MnO_2-1: black line; MnO_2-200: red line; MnO_2-300: blue line; MnO_2-400: dark cyan line). (For interpretation of the references to color in this figure legend, the reader is referred to the web version of this article.)

AC–MnO_2-300&AC show rectangular shapes without noticeable redox peaks in 1.8 V operating windows, while the hybrid supercapacitor AC–MnO_2-0&AC slightly deviated from the ideal rectangular shape.

Fig. 9b shows the voltage *vs* time profile of the hybrid AC–MnO_2&AC aqueous hybrid supercapacitor at a current density of 6 mA cm^{-2}. The potential *vs* time curves of the AC–MnO_2-1&AC, AC–MnO_2-200&AC and AC–MnO_2-300&AC exhibit almost linear shapes due to their fast pseudo-capacitive nature (as the mass of the AC–MnO_2-200 and AC–MnO_2-300 electrode slices are bigger than AC–MnO_2-1, so the discharge times of AC–MnO_2-200 and AC–MnO_2-300 are longer than AC–MnO_2-1), while the hybrid supercapacitor AC–MnO_2-0&AC shows a sloping voltage profile from 0 to 1.8 V operating windows with a distinct voltage drop caused by the internal resistance (*IR*). We know *IR* is associated with the equivalent series resistance of the supercapacitor cell. The *IR* drop values for AC–MnO_2-1&AC, AC–MnO_2-200&AC and AC–MnO_2-300&AC are negligible. However, a large voltage drop is evident for AC–MnO_2-0&AC, indicating the large inner resistance of the electrode material. The weakness of AC–MnO_2-0&AC may be ascribed to the morphology and structure of the bulk MnO_2-0, which also belongs to δ-phase but has low surface area and pore volume. This results in a large internal resistance.

Fig. 10 shows the cycling behavior of the hybrid AC–MnO_2-0&AC, AC–MnO_2-1&AC, AC–MnO_2-200&AC and AC–MnO_2-300&AC supercapacitor in 0.5 M Na_2SO_4 electrolyte at a large current

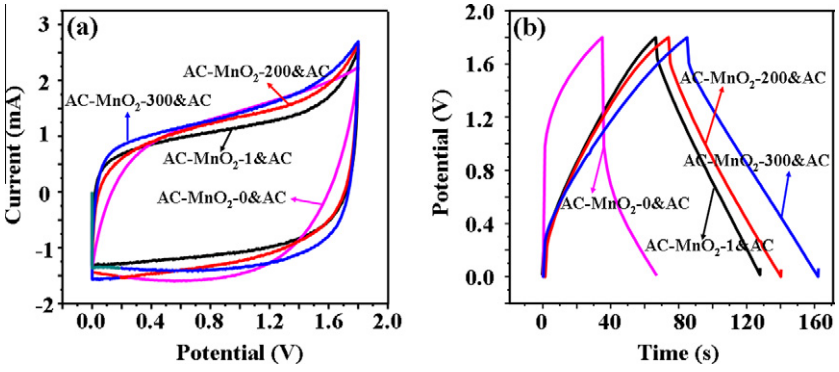

Fig. 9. (a) Cyclic voltammograms (b) potential *vs* time curves of the optimized hybrid AC–MnO_2-0&AC (magenta line), AC–MnO_2-1&AC (black line), AC–MnO_2-200&AC (red line) and AC–MnO_2-300&AC (blue line) capacitor in 0.5 M Na_2SO_4 aqueous solution. (For interpretation of the references to color in this figure legend, the reader is referred to the web version of this article.)

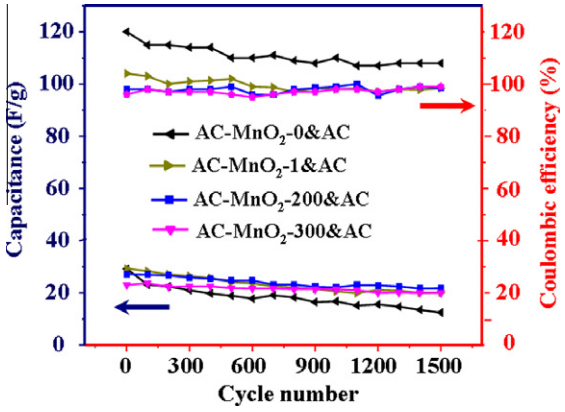

Fig. 10. Cycling behavior of the hybrid AC–MnO_2-0&AC, AC–MnO_2-1&AC, AC–MnO_2-200&AC, AC–MnO_2-300&AC and coulombic efficiency (CE) of the hybride supercapacitors AC–MnO_2-0&AC, AC–MnO_2-1&AC, AC–MnO_2-200&AC and AC–MnO_2-300&AC at a current density of 0.01 A between 0 and 1.8 V.

density of 12.74 mA cm^{-2} between 0 and 1.8 V. There is a slight decline in capacitance for the first 200 cycles, which may be due to the activation and stability process of the electrode, gradually reaching a steady-state. We did not take any measures to remove the dissolved oxygen from the electrolyte, which will decrease the cycling stability of the electrodes [15]. It can be seen that in high current density cycling, the disadvantages of the hybrid AC–MnO_2-0&AC supercapacitor is obvious, with a serious in the capacity. In contrast, the AC–MnO_2-1&AC supercapacitor shows an improved cycling behavior. This can be attributed to the presence of mesopores in sample MnO_2-1. There are no significant differences in the results of the three-electrode tests, but clear difference can be seen in the two-electrode tests. This may be because the three-electrode test uses a platinum electrode as counter electrode, which has good conductivity and stability. If the conductivity of a single electrode is poor, the potential drop of internal resistance of the capacitor will be obvious. Moreover, calcined samples (AC–MnO_2-200&AC, AC–MnO_2-300&AC) have more stable electrochemical properties, with a 22.1 F g^{-1} (calculated based on the total mass of the two active electrode materials) capacity retained after 1500 cycles. The coulombic efficiency of all of the hybrid capacitors with the exception of AC–MnO_2-0&AC, remain at 100% apart from the first several cycles, suggesting that no gas evolution occurred over this voltage range. While the coulombic efficiency of AC–MnO_2-0&AC still above 100% even after 1500 cycles, this may be due to side reactions [23]. The good behavior of AC–MnO_2-200&AC supercapacitor can be ascribed to the large pore volume and high surface area, with abundant mesopores embedded in the electrode materials.

4. Conclusions

In this study, a series of mesoporous manganese dioxides was obtained through a one-pot reaction at ambient conditions from $KMnO_4$ and ethylene glycol under acidic conditions. The presence of the acid altered both the morphology and the structure of the MnO_2. The crystalline structure changed from δ- to α-phase accompanied by a change of the support ion concentration. The specific surface area and pore volume of the acid-treated samples were significantly increased, together with a decrease in the average pore size. MnO_2 prepared under acidic conditions can maintain its α-phase crystalline structure after a heat treatment of 200 °C and still possess a high surface area (159 m^2 g^{-1}) and large pore volume (0.66 cm^3 g^{-1}) after 300 °C heat treatment. A hybrid supercapacitor formed with a manganese oxide based positive electrode and activated carbon based negative electrode has been prepared and shows a capacitive performance of 22.1 F g^{-1} after 1500 cycles. The excellent electrochemical properties of MnO_2 prepared under acidic conditions are attributed to its mesoporous structure as well as its high surface area and large pore volume.

Acknowledgement

We would like to thank the financial support by Program for the National Natural Science Foundation of China (No. 20973031).

References

[1] G.G. Amatucci, F. Badway, A.D. Pasquier, T. Zheng, J. Electrochem. Soc. 148 (2001) A930.
[2] A. Du Pasquier, A. Laforgue, P. Simon, J. Power Sources 125 (2004) 95.
[3] B.E. Conway, J. Electrochem. Soc. 138 (1991) 1539.
[4] B.E. Conway, V. Birss, J. Wojtowicz, J. Power Sources 66 (1997) 1.
[5] J. Zheng, T.R. Jow, J. Electrochem. Soc. 142 (1995) L6.
[6] R. Kötz, M. Carlen, Electrochim. Acta 45 (2000) 2483.
[7] M. Toupin, T. Brousse, D. Bélanger, Chem. Mater. 14 (2002) 3946.
[8] C.-C. Hu, T.-W. Tsou, Electrochem. Commun. 4 (2002) 105.
[9] V. Subramanian, H. Zhu, B. Wei, J. Power Sources 159 (2006) 361.
[10] C. Yu, L. Zhang, J. Shi, J. Zhao, J. Gao, D. Yan, Adv. Funct. Mater. 18 (2008) 1544.
[11] R. Liu, S.B. Lee, J. Am. Chem. Soc. 130 (2008) 2942.
[12] J.B. Fei, Y. Cui, X.H. Yan, W. Qi, Y. Yang, K.W. Wang, Q. He, J.B. Li, Adv. Mater. 20 (2008) 452.
[13] H. Chen, J. He, J. Phys. Chem. C 112 (2008) 17540.
[14] M.S. Hong, S.H. Lee, S.W. Kim, Electrochem. Solid-State Lett. 5 (2002) A227.
[15] T. Brousse, P.-L. Taberna, O. Crosnier, R. Dugas, P. Guillemet, Y. Scudeller, Y. Zhou, F. Favier, D. Bélanger, P. Simon, J. Power Sources 173 (2007) 633.
[16] T. Brousse, M. Toupin, D. Bélanger, J. Electrochem. Soc. 151 (2004) A614.
[17] P.-C. Gao, A.-H. Lu, W.-C. Li, J. Power Sources 196 (2011) 4095.
[18] Y.T. Wang, A.-H. Lu, W.C. Li, J. Phys. Chem. C 115 (2011) 5413.
[19] X.-F. Shen, Y.-S. Ding, J. Liu, J. Cai, K. Laubernds, R.P. Zerger, A. Vasiliev, M. Aindow, S.L. Suib, Adv. Mater. 17 (2005) 805.
[20] S.W. Donne, A.F. Hollenkamp, B.C. Jones, J. Power Sources 195 (2010) 367.
[21] C. Lin, J.A. Ritter, B.N. Popov, J. Electrochem. Soc. 146 (1999) 3155.
[22] V. Khomenko, E. Raymundo-Piñero, F. Béguin, J. Power Sources 153 (2006) 183.
[23] H. Mukaibo, T. Sumi, T. Yokoshima, T. Momma, T. Osaka, Electrochem. Solid-State Lett. 6 (2003) A218.